Loss Analysis of a Bearingless Flux-Switching Slice Motor

Karlo Radman [a], Wolfgang Gruber [b], Neven Bulić [a]

[a] University of Rijeka, Vukovarska 58, 51000 Rijeka, Croatia, karlo.radman@riteh.hr, neven.bulic@riteh.hr
[b] Johannes Kepler University Linz, Altenberger Str. 69, 4040 Linz, Austria, wolfgang.gruber@jku.at

***Abstract*—The bearingless flux-switching slice motor is a recently developed motor concept combining the magnetic rotor suspension of a bearingless slice drive and the topology of a flux-switching drive. In comparison to state of the art bearingless slice motors this concept introduces a magnet free rotor and relatively high torque generation. This offers advantages in industrial and medical applications which require regular rotor replacements and high temperature working conditions. This work will describe the working principles, prototype design, implemented control theory and measurement to determine the losses and evaluate the efficiency.**

I. Introduction

Bearingless motors refer to electrical drives in which torque and the bearing forces are generated by one integrated motor element. Stator coils create both motor torque and radial bearing forces. The remaining degrees of freedom, of the rotor, can be passively stabilized by including a permanent magnetic bias flux in the air gap and a disc shaped rotor, as depicted in Fig. 1. With the additional actively controlled radial deflection, a fully magnetically suspended rotor is achieved. Such integrated levitating drives were developed in the mid 90's and are known as "bearingless slice motors" [1]. Bearingless slice motors are used in medical, pharmaceutical and semiconductor industry due to low vibrations and the ability to hermetically seal the rotor [2], [3].

In chemical and medical applications where the rotor is regularly replaced because of contamination, permanent magnets (PM) embedded in the rotor significantly increase the disposable rotor price. The working temperature conditions also limit the use of PM, and for such applications a magnet free rotor topology is preferable. The flux-switching permanent magnet (FSPM) motor topology solves that issue by placing the PM on the stator iron. The rotor is therefore reduced to a salient laminated steel ring. Two variants of the bearingless reluctance slice drives, without PM on the rotor, were recently proposed [4]. The first variant has a constant directional homopolar PM field, while the bearingless flux-switching drive represents the heteropolar version with an alternating PM field in the air gap.

This paper describes the working principle, control scheme and design of a bearingless flux-switching slice motor. A finished prototype was put into operation and the characteristics were measured to determine the eddy current losses and the overall efficiency of the motor. Three-dimensional finite element (3D FEM) simulations were compared to measurement results and show an acceptable congruence.

II. Bearingless Flux-Switching Motor

A. Flux-Switching Permanent Magnet Motor

The topology of a FSPM motor is shown in Fig. 2. The tangentially polarized permanent magnets are situated in each stator teeth and adjacent magnets have opposing directions (depicted in red and green in Fig. 2). This configuration separates the stator electromagnetically, in such a manner that the magnetic flux from each tooth is closing only over the two neighboring ones. With an even rotor and stator teeth number a symmetric layout is achieved with opposing coils having in phase induced voltages.

Due to the rotor saliency, an alternating angle depended linked flux is observed in the stator coils. A sinusoidal back-electromotive force is induced and linear PM torque generation is possible. Figure 3 illustrates the maximum PM flux entering the rotor, at an electrical rotor angle of 90° and 270° teeth. The PM flux is changing its direction over the electrical rotor angle and the direction switch occurs at 0° and 180° electrical.

B. Torque and Force Generation

The stator coil field superimposed on the PM field leads to local field weakening and strengthening which in turn exerts force on the rotor, as shown in Fig 3. Each coil is capable of generating both force and torque and for controlled magnetically suspended rotor operation, force and torque generation need to be decoupled. Additionally, radial bearing force needs to be linearly current dependent for the position control. Because of the motor symmetry, the opposing rotor coils can be connected in series, shown in Fig 4. If the fields

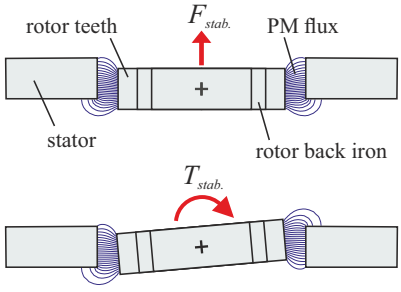

Figure 1. Passive stabilisation of axial deflection (top) and tilting (bottom) in bearingless slice drives.

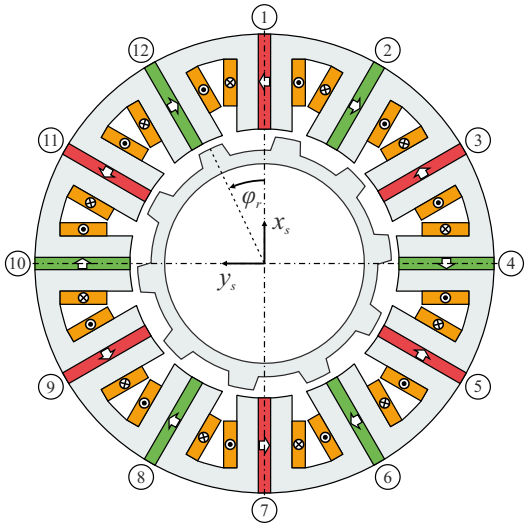

Figure 3. Topology of a FSPM drive

of both coils are oriented in the same direction, torque and all quadratic force components cancel out and linear force generation is achieved. Vice versa, with the coil fields pointing in opposing direction the force generation cancels out. This way, with different connections of the opposing coils a phase with decoupled linear torque or force generation is possible.

Figure 5 depicts a characteristic torque and force generation of a single phase energized with constant current over the electrical rotor angle. Torque is generated by the phase with concordantly connected coils, while radial force with inversely connected opposing coils. Maximal force normal to the phase is generated at a rotor electrical angle of 90° and 270° when the maximal PM field is closing over the rotor teeth. Similarly maximum torque is achievable at 0° and 180° degrees electrical. Tangential force angle dependency is in phase with the torque generation. A force phase is

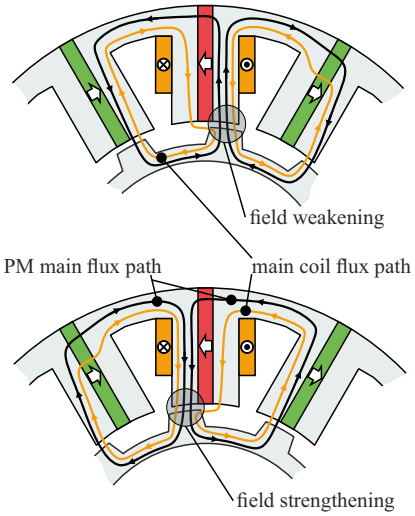

Figure 2. Basic principle of the switching flux path of a motor segment. additional field strengthening (top), and weakening (bottom) applied with a constant current and varying electrical rotor angle (-90°el. top, +90°bottom)

generating negligible torque while the torque phase is not creating any significant force on the rotor.

C. Passive stabilization

The PM field from each stator segment exerts reluctance forces to minimize the air gap. Reluctance forces in radial direction pull the rotor away from the center operating position, and are therefore destabilizing. The reluctance forces, in axial direction, strive to achieve position with minimal air gap length by aligning the rotor in plane with the stator, thus, stabilizing the axial displacement, as shown in Fig. 1 (top). Figure 1 (bottom) depicts the same principle that stabilizes the *x*- and *y*-axis tilting.

If the rotor is constructed with a relatively small height in regard to the diameter, a bearingless slice motor operation is viable, with three degrees of freedom passively stabilized [5]. At any rotor angle, with a high rotor/stator teeth number, there is always some rotor teeth over which the PM flux is closing, and therefore the axial stabilization force and *x*- and *y*-axis tilting stabilizing torque have a mostly constant term over the rotor angle, Figure 6 shows the 3D FEM simulated passive forces and torque for a full electrical rotor angle.

III. PROTOTYPE DESIGN AND CONTROL

A. Mathematical model

Each stator coil is capable of creating drive torque T_z, and normal and tangential bearing force relative to the coil. The overall suspension forces F_x and F_y, in a stator fixed coordinate system and the motor torque T_z for the whole motor can be expressed over the phase current vector $\boldsymbol{i_s}$ as [5]

$$\begin{pmatrix} F_x(\varphi_r) \\ F_y(\varphi_r) \\ T_z(\varphi_r) \end{pmatrix} = \begin{pmatrix} \boldsymbol{i_s}^T & 0 & 0 \\ 0 & \boldsymbol{i_s}^T & 0 \\ 0 & 0 & \boldsymbol{i_s}^T \end{pmatrix} \boldsymbol{T}_Q(\varphi_r)\boldsymbol{i_s} + \boldsymbol{T}_L(\varphi_r)\boldsymbol{i_s} + \boldsymbol{T}_C(\varphi_r) \qquad (1)$$

with φ_r being the mechanical rotor angle. Centered rotor position is assumed. The mathematical model is valid only for linear material behaviour. Saturation effects are not considered and the motor is therefore expected to work below saturation levels in the laminated steel. The term $\boldsymbol{T}_C$, describing cogging torque and purely PM reluctance forces, is relatively small in FSPM drives they work on the principle of PM synchronous machines, opposed to the reluctance machines usually

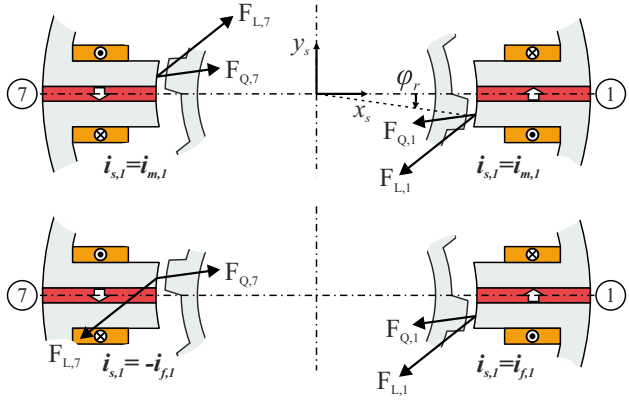

Figure 4. Decoupling of force and torque by different in series winding connections. Winding connection for torque generation (top) and connection for force generation (bottom)

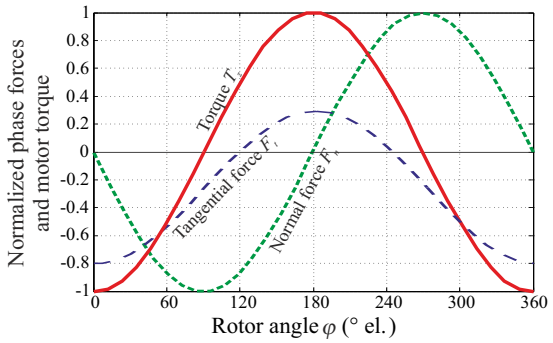

Figure 5. Normalized values generated by single DC energized stator phases over the electrical rotor angle. Torque generated by a torque phase and forces normal and tangential to a force phase.

connected to magnet-free rotors. With 12 stator and 10 rotor teeth and optimum rotor teeth width, the reluctance torque and higher harmonics influences can be minimized, as research shows for conventional FSPM drives [6], [7]. $\boldsymbol{T}_Q$ is the quadratic term influenced by the stator currents alone, without the PM. It is the dominant element in classic magnetic bearings and reluctance machines. The linearly current depended vector $\boldsymbol{T}_L$ represents the forces and torque that are created due to the interaction between the PM field and stator current field. This part is dominant in PM machines and is the only desirable element in the mathematical model (1), since a decoupling of torque and force generation has to be obtained based on linear superposition.

With the already mentioned series connection of opposing coils the quadratic current dependent terms $\boldsymbol{T}_Q$ are superimposed and the linear force and torque model of a bearingless flux-switching motor is

$$\begin{pmatrix} F_x(\varphi_r) \\ F_y(\varphi_r) \\ T_z(\varphi_r) \end{pmatrix} = \boldsymbol{T}_L(\varphi_r)\boldsymbol{i}_s. \qquad (2)$$

For a stator with 12 segment, which make six phases, the phase current vector can be defined as

$$\boldsymbol{i}_s=(i_1 \quad i_2 \quad i_3 \quad i_4 \quad i_5 \quad i_6)^{\mathrm{T}}. \qquad (3)$$

The optimal wiring topology and distribution of torque and force phases has been researched [8]. A three-phase system is used for the torque generation, as found in consecutive pole wound flux-switching machines [9]. The remaining three phases, shifted 120°, generate the radial suspending forces. The phase topology is presented in Table I and follows the winding directions marked in Fig. 2. The force and torque orbit of a 2x3-phase system is shown in Fig. 7. The orbits are calculated from the waveforms in Fig 5.

TABLE I. PROTOTYPE PHASE TOPOLOGY

Phase	Generation of	First Coil		Second coil	
No.		No.	Current	No.	Current
1	Force	1	i_1	7	$-i_1$
2	Torque	2	i_2	8	i_2
3	Force	5	i_3	11	$-i_3$
4	Torque	6	i_4	12	i_4
5	Force	9	i_5	3	$-i_5$
6	Torque	10	i_6	4	i_6

B. *Control system*

Equation (2) is used to calculate the pseudo inverse control matrix $\boldsymbol{K}_m$.[10]

$$\boldsymbol{K}_m(\varphi_r)=\boldsymbol{T}_L(\varphi_r)^{\mathrm{T}}\left(\boldsymbol{T}_L(\varphi_r)\,\boldsymbol{T}_L(\varphi_r)^{\mathrm{T}}\right)^{-1}. \qquad (4)$$

The nonlinear control matrix $\boldsymbol{K}_m$ gives the relation between suspension forces, drive torque, and therefore needed phase currents with the lowest possible resistive copper losses. The phase currents can be calculated from

$$\boldsymbol{i}_s = \boldsymbol{K}_m(\varphi_r)(F_x \quad F_y \quad T_z)^T \qquad (4)$$

for given reference suspension forces and drive torque. $\boldsymbol{K}_m$ can be implemented in the control system with feedback control loops for position and torque. Matrix $\boldsymbol{T}_L$ needed for (4) is calculated from the characteristic waveforms in Fig 5, which can be obtained from FEM simulations.

Due to symmetrical attraction from all sides, passive destabilizing radial reluctance forces are minimal in the central position. When the magnetic air gap is the same from all sides, only little force is needed to maintain the rotor levitating. An additional control loop for finding the reference central position is implemented. A relatively slow integration of the *x*- and *y*-position controller output can be fed back instead of a constant reference value. This zero-force control feedback loop enables the self calibration of the position

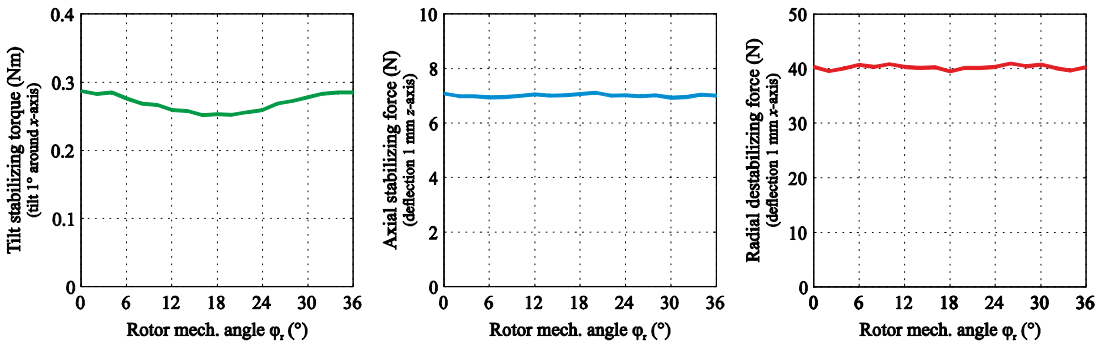

Figure 6. Prototype 3D FEM simulated passive rotor stiffness. Tilting stabilizing torque at a rotor tilt of 1° around the x-axis (left), axial stabilizing force at 1 mm axial rotor displacement (center), and radial destabilizing force at an radial *x*-axis displacement of 1 mm (right)

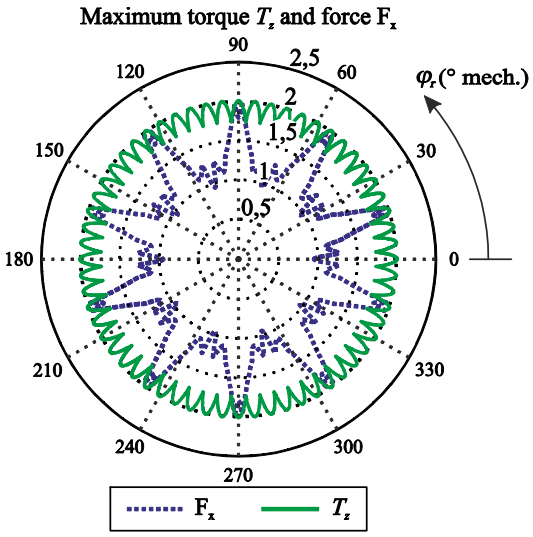

Figure 7. Orbit plots for maximum producible motor torque and bearing forces. Values are relative to the maximum per phase producible torque/force, as seen Fig. 5. Orbits are created by separate three-phase torque and force systems.

references for bearingless operation. The control scheme is depicted in Fig. 8.

Position is measured using four eddy currents sensors around the stator circumference. The sensor coil field is influenced by the induced currents in a thin aluminum layer around the rotor. Position in x- and y-axis is measured differentially with two opposing sensor coils. Rotor angle measurement is made with a three-phase Hall sensor arrangement between the stator segments, that measure the sinusoidal PM flux change over the rotor angle.

C. Prototype

A bearingless flux-switching slice motor prototype was optimized and built to validate the simulated model [11]. Optimizations were made using 3D FEM simulations. Criterions included adequate axial and tilting stiffness and motor operating point below iron saturation limits. Additional parameters regarding pole pair number, pitch ratio and the motor split ratio were chosen based on research of conventional flux-switching machine with bearings [6], [7]. The prototype in two assembly stages is shown in Fig. 9, and the main parameters are given in Table II.

The electronic part includes a 2 KW power inverter, with two three-phase half bridges. The control was implemented on a TI DSP using the X2C toolbox developed by the Linz Center of Mechatronic (LCM) [12]. Force and torque phase coils have the same number of windings, which is 80 per coil, and thus 160 per phase. Phase resistance equals 0.86 Ω.

TABLE II. PROTOTYPE PARAMETERS

Parameter	Value	Unit
stator iron outer diameter	266	mm
rotor outer diameter	150	mm
rotor and stator height	10	mm
magnetic air gap	3	mm
magnet width	8,5	mm
magnet length	54	mm
laminated iron material	M330-35A	
PM material	NdFeB N38	

IV. MEASUREMENTS

The assembled prototype was put into operation and static measurements were carried out. Forces in radial and axial direction, and motor torque were measured on a test bench. Static measurements were made with a force and torque load cell for a full electrical angle. Linearity of the force generation for a single phase can be seen in Fig. 10. Saturation affects the force generation above phase current of 10A, which is a magnetomotive force of 1600 Aturns. Figure 11 shows the force orbit of a single force phase energized with constant 9.5 A. The static simulated and measured data can be seen in Table III. Passive and actively generated electromagnetic characteristics show deviation around 10% from the simulation data, which can be contributed to the nonideal PM.

Dynamic measurement where conducted with the rotor mechanically attached to the torque sensor and test load. Suspension control was turned off, and only the torque phases were used. As the torque phases are separated by force phases in between them, cross coupling between torque phases is not present. This is due to the coil flux closing only over adjacent stator segments, as depicted for two rotor angles in Fig. 3.

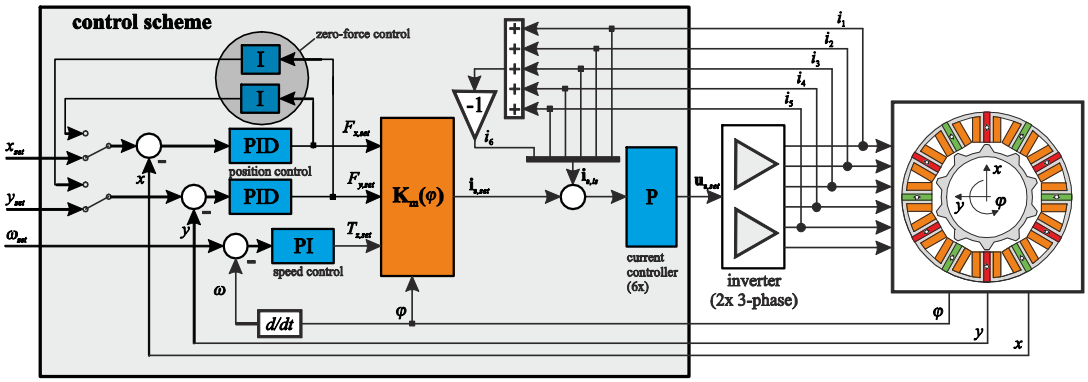

Figure 8. Control scheme of a bearingless flux-switching slice drive

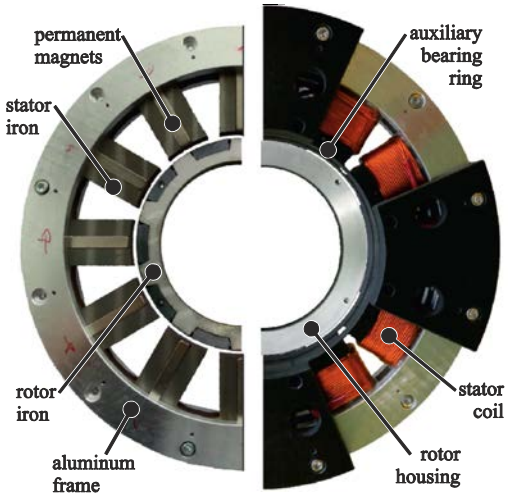

Figure 9. Half (left) and fully (right) assembled prototype.

TABLE III. SIMULATED AND MEASURED ELECTROMAGNETIC CHARACTERISTICS

Parameter	Simulated	Measured	Unit
Radial stifness	20.8	18	N/(0.5mm)
Axial stiffness	7.25	7.04	N/mm
Tilt stifness	21.4	NA	Nm/rad
Bearing force (phase, peak, at 9.5 A)	26.4	26	N
Drive torque (phase, peak, at 9.5 A)	0.708	0.66	Nm
Induced phase voltage constant (peak)	0.08	0.0757	V/(rad/s)
Max. current density	6		A/mm^2

When the motor is running in horizontal position, the rotor is axially displaced do to its weight. The prototype rotor weights 700 g and is displaced approximately 1 mm. The RMS induced phase voltage in reference to axial displacement, at a rotor speed of 500 rpm, is shown in Fig 12. With increasing axial displacement the motor torque is decreasing.

Cogging torque and lo load was measured with the test load spinning the rotor and the result are shown in Fig. 13.

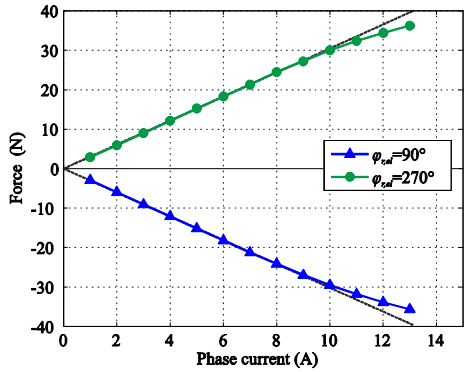

Figure 10. Force generation of a DC energized force phase.

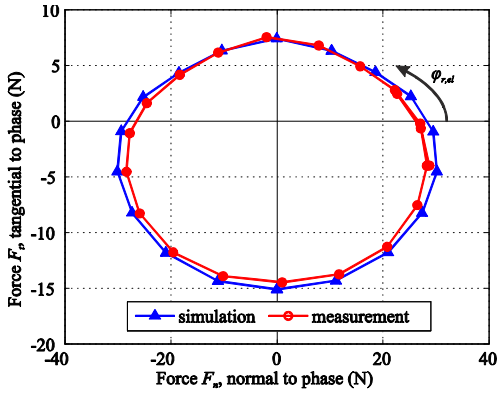

Figure 11. Measured and simulated force orbit of a single DC energized force phase for a full electrical rotor angle. Constant magneto-motive force of 1520 Aturns.

The aluminum 0.5 mm thick rotor housing needed for position measurements has been proven to create enormous eddy current losses. At a rotor speed of 1000 rpm the eddy current losses reach 180 W, which significantly increase the rotor temperature. For that reason, all measurements were done with a nonconductive rotor housing, as the position measurement was not needed with a mechanically suspended rotor. Measured cogging torque at lower speeds is about 12 mNm and the no load free-wheel losses at 1000 rpm are 3.12 W. These measurements prove the used optimization and that the bearingless flux-switching slice drive, although having a rotor similar to reluctance machines, is lacking the characteristic cogging torque.

Figure 14 shows the measurement of real, complex and motor output power at 1000 rpm. Due to the high stator coil inductivity the power factor is around 0.22 at the load of 1.55 Nm. Efficiency at different speeds is shown in Fig 15. Linearly and quadratic frequency dependent losses are not dominant and most losses are resistive heating. Therefore as the speed increases, the motor output power is rising in reference to the real electrical power, and the efficiency also increases.

V. CONCLUSION

The bearingless flux-switching slice motor concept was successfully realized into a working prototype and the first measurements satisfactorily coincide with the expected 3D

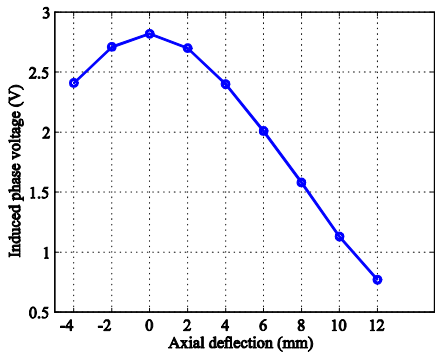

Figure 12. RMS induced phase voltage at 500 rpm for varying axial deflection.

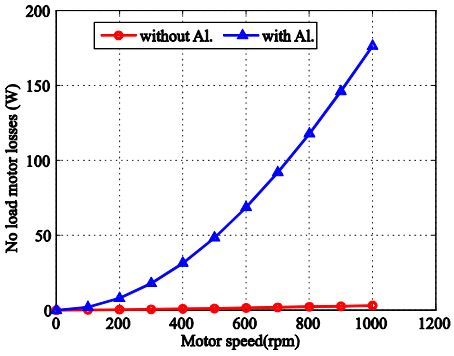

Figure 13. No load motor losses with and without the aluminum rotor housing. Eddy current losses in are quadratic dependent with the frequency.

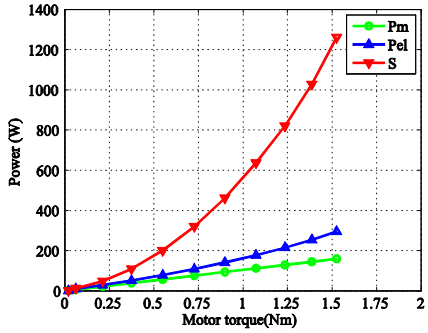

Figure 14. Measured motor, real and complex power at 1000 rpm. Due to high inductivity the power factor at maximum load is 0.22.

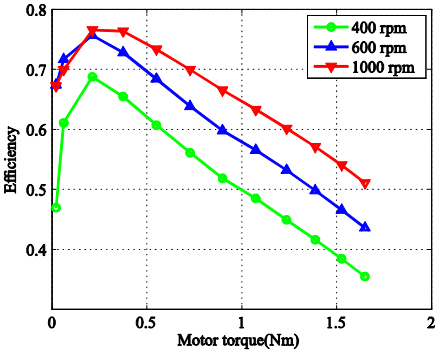

Figure 15. Motor efficiency at different speeds. The efficiency is increasing with motor speed.

FEM simulation results. The high losses of the position measurement aluminum housing have to be removed by finding new solutions for position measuring sensors in the next prototype. With a new position sensor solution, measurements of bearingless operation under varying load and speed would be measurable. Saturation levels in iron where found at expected levels at the rated motor current of 10A. The cogging torque was proven to be minimal, and neither the torque or force orbit has a single phase characteristic. Further step are taken to increase the motor stability and drive torque generation by increasing the motor height.

VI. ACKNOWLEDGMENT

Parts of this work were supported by the Linz Center of Mechatronics (LCM) GmbH, a K2-centre of the COMET program of the Austrian Government. The authors thank the Austrian and Upper Austrian Government for their support.

REFERENCES

[1] Schöb, R., Barletta, N., "Principle and application of a bearingless slice motor," Proc. 5th Int. Symp. on Magnetic Bearings (ISMB), pp. 333-338, 1996

[2] Salazar, A. Chiba, and T. Fukao. "A review of developments in bearingless motors," In Proceedings of ISMB7, 2000

[3] Warberger, B.; Kaelin, R.; Nussbaumer, T.; Kolar, J.W., "50 Nm/2500-W Bearingless Motor for High-Purity Pharmaceutical Mixing," Industrial Electronics, IEEE Transactions on, vol.59, no.5, pp. 2236-2247, May 2012

[4] Gruber, W.; Briewasser, W.; Rothbock, M.; Schob, R.T., "Bearingless slice motor concepts without permanent magnets in the rotor," Industrial Technology (ICIT), 2013 IEEE International Conference on, pp. 259-265, 25-28 Feb. 2013

[5] Schöb, R., Barletta, N., "Principle and Application of a Bearingless Slice Motor," Proc. 5th Int. Symp. on Magnetic Bearings (ISMB), pp. 333-338, 1996

[6] Chen, J.T.; Zhu, Z.Q., "Winding Configurations and Optimal Stator and Rotor Pole Combination of Flux-Switching PM Brushless AC Machines," Energy Conversion, IEEE Transactions on , vol.25, no.2, pp. 293-302, June 2010

[7] Wei Hua; Ming Cheng; Zhu, Z.Q.; Howe, D., "Analysis and Optimization of Back-EMF Waveform of a Novel Flux-Switching Permanent Magnet Motor", Electric Machines & Drives Conference, 2007. IEMDC '07. IEEE International, vol.2, pp.1025-1030, 3-5 May 2007

[8] Gruber, W., Bauer, W., Radman, K., Amrhein, W. and Schöb, T., "Considerations Regarding Bearingless Flux-Switching Slice Motors", Proceeding on 1st Brazilian Workshop on Magnetic Bearings, 2013

[9] Owen, R.L.; Zhu, Z.Q.; Thomas, A.S.; Jewell, G.W.; Howe, D., "Alternate Poles Wound Flux-Switching Permanent-Magnet Brushless AC Machines," Industry Applications, IEEE Transactions on , vol.46, no.2, pp. 790-797, March-April 2010

[10] Silber, S., Amrhein, W., "Power Optimal Current Control Scheme for Bearingless PM Motors", Proc. 7 th Int. Symp. on Magnetic Bearings (ISMB), pp. 401-406, 2000

[11] Gruber, W, Radman, K., Schöb, R., "Design of a Bearingless Flux-Switching Slice Motor", Proc. Int. Power Elec. Conf. (IPEC), 2014, in press

[12] Radman, K.., Gruber, W., Bulić, N., "Control Design of a Bearingless Flux-Switching Slice Drive", European Embedded Design in Education and Research Conference (EDERC), 2014, in press